Journal of Crystal Growth 379 (2013) 84–92

Contents lists available at SciVerse ScienceDirect

Journal of Crystal Growth

journal homepage: www.elsevier.com/locate/jcrysgro

Point defects in Cd(Zn)Te and TlBr: Theory

Vincenzo Lordi *

Lawrence Livermore National Laboratory, 7000 East Avenue, L-413, Livermore, CA 94550, USA

ARTICLE INFO

Available online 13 March 2013

Keywords:
A1. Computer simulation
A1. Diffusion
A1. Doping
A1. Point defects
B1. Halides
B2. Semiconducting materials

ABSTRACT

The effects of various crystal defects on the performances of CdTe, $Cd_{1-x}Zn_xTe$ (CZT), and TlBr for room-temperature high-energy radiation detection are examined using first-principles theoretical methods. The predictive, parameter-free, atomistic approaches used provide fundamental understanding of defect properties that are difficult to measure and also allow rapid screening of possibilities for material engineering, such as optimal doping and annealing conditions. Several recent examples from the author's work are reviewed, including: (i) accurate calculations of the thermodynamic and electronic properties of native point defects and point defect complexes in CdTe and CZT; (ii) the effects of Zn alloying on the native point defect properties in CZT; (iii) point defect diffusion and binding leading to Te clustering in Cd(Zn)Te; (iv) the profound effect of native point defects—principally vacancies—on the intrinsic material properties of TlBr, particularly its electronic and ionic conductivity; and (v) a study on doping TlBr to independently control the electronic and ionic conductivity.

© 2013 Elsevier B.V. All rights reserved.

1. Introduction

1.1. Room-temperature radiation detectors

Cadmium telluride (CdTe), cadmium zinc telluride (CdZnTe), and thallium bromide (TlBr) are promising semiconducting materials for high-performance high-energy radiation detectors operating at room temperature. Such detectors, when able to resolve the energy of incoming gamma- or X-rays to better than 1% at characteristic energies, find important uses in applications including nuclear nonproliferation, homeland security, medical imaging, and space imaging [1–3]. The performance of the radiation detector ultimately depends on the active semiconductor material—both its intrinsic properties and the quality of a given crystal [4,2,5]. Several material properties dictate the performance of a semiconductor crystal for high energy-resolution room-temperature radiation detection, stemming from the operation principle of direct conversion of incoming photons to electrical current. Energy resolution is achieved when the measured current is proportional to the photon energy. The efficiency and energy resolution of the detector thus depend on its ability to absorb high-energy photons, generate free carriers, and create an externally measurable current proportional to the photon energy. Large single crystals on the order of 1 cm^3 or larger are usually required to achieve maximum absorption of radiation in the 10–10,000 keV range. A large voltage, typically on the order of 1000 V and limited by the dielectric breakdown of the crystal, is applied to the detector to create a maximal electric field to sweep out the photogenerated carriers to count the photocurrent.

The following material properties are crucial for maximizing the signal-to-noise ratio and achieving high-performance radiation detection at room temperature. First, materials containing high-Z elements ($\gtrsim$50) are desired to maximize sensitivity and minimize the required volume, since photoelectric absorption of high energy radiation varies as Z^5. Second, a small band gap is desired, since the number of photogenerated carriers is proportional to the ratio of photon energy to the band gap; however, too small a band gap contributes noise from thermal excitation of carriers across the gap. In practice, a band gap of ~1.4–2.2 eV is suitable for room-temperature operation, with ~1.6 eV nearly optimal. Similarly, high resistivity is required to avoid noise from a large Ohmic background current. Finally, the carrier drift length, which is proportional to the product of carrier mobility and carrier trapping lifetime, is required to be on the order of 1–10× the distance between electrical contacts to ensure complete collection of photogenerated carriers and thus linearity between photon energy and measured current. This final requirement is essential for high energy resolution, and semiconductor radiation detector materials are typically characterized by the figure of merit $\mu\tau$, the product of mobility and lifetime, with a desired target $\gtrsim 10^{-2}$ cm^2/V.

As mentioned above, both intrinsic and extrinsic properties of a crystal affect its performance. Defects of various scales in the material, from point defects to defect complexes to aggregates/precipitates to dislocations and grain boundaries, can sensitively affect the electronic properties, particularly mobility, lifetime, and

* Tel.: +1 925 423 2755.
E-mail address: lordi2@llnl.gov

0022-0248/$ - see front matter © 2013 Elsevier B.V. All rights reserved.
http://dx.doi.org/10.1016/j.jcrysgro.2013.03.003

resistivity. Therefore, maximal detector performance is achieved through control of defects (e.g., purification and single-crystal growth) and engineering the distribution of desired defects (e.g., doping).

This paper will examine the role of various relevant defects in two specific room-temperature radiation detection materials, Cd(Zn)Te and TlBr, reviewing several examples from our recent work [6–11]. The analyses will rely on theoretical assessments of the distribution of different defects and their effects on transport properties, with connections to experimental results made as appropriate. Simulations based on parameter-free first-principles atomistic-scale models provide predictive power to understand the role of defects on material performance without input from experiments. This predictive approach enables not only the understanding of fundamental defect properties which are difficult to measure directly, but also rapid virtual screening of a large number of scenarios (e.g., potential dopants, growth conditions, annealing conditions, etc.) to guide development and optimization of real materials.

Both $Cd_{1-x}Zn_xTe$ (CZT) and TlBr are materials that nominally meet the criteria outlined above for high-performance room-temperature radiation detectors, but each is limited by different defect-related effects that must be overcome or managed.

1.2. Cd(Zn)Te

CdTe has been demonstrated as a good radiation detector material, with high-purity crystals exhibiting high $\mu\tau$ products (up to 3×10^{-3} cm^2/V at room temperature) and high resistivity (up to 10^9 Ω cm) [12,2,4,13]. For the highest performance detectors at room temperature, Zn is added to increase the band gap from 1.5 to ~1.6 eV (with ~10% Zn), which reduces thermal noise and increases the resistivity up to 8×10^{10} Ω cm [14,2,13]. Additional empirical benefits of Zn alloying in CdTe include oxygen gettering, increased hardness, and reduced "polarization" effect (time-dependent detector degradation due to internal fields from charge separation) [2]. CZT gamma detectors have achieved energy resolution better than 1% at 662 keV [15,16] (a resolution benchmark), but material costs are high from the difficulty of growing large uniform single crystals and the typical need for crystal harvesting. (CdTe and CdTe-based alloys also find important applications in solar cells and optical modulators, where much smaller volumes are required.) A variety of crystal defects—ranging from point defects to inclusions/precipitates/secondary phases to dislocations and grain boundaries—limit the performance of individual crystals. Generally, defects that trap carriers and reduce the carrier lifetime are the most detrimental. We will examine theoretically the properties and effects of several of these defects below.

1.3. TlBr

TlBr also has demonstrated outstanding performance for room-temperature gamma detection, with resolution better than 1% at 662 keV [17–19]. The high performance stems from the large band gap (2.7 eV), long carrier lifetime (up to 10^{-4} s), and high resistivity (~10^{11} Ω cm at 298 K). However, a major practical problem is that detector performance degrades over times that vary from hours to several weeks [20,21], a phenomenon termed "polarization." Point defects, particularly vacancies, play a major role in this phenomenon and also contribute to some of the favorable properties of the material. Below, we examine their roles in detail and suggest defect engineering strategies to improve TlBr detector stability.

2. Methods

Density functional theory (DFT) is used as the basis for our analyses. We employ the supercell approximation and the projector augmented-wave (PAW) method [22,23]. Outside the PAW core regions, wavefunctions are expanded in a plane-wave basis [24–27]. Various approximations for the exchange-correlation are used, including the local density approximation (LDA) [28,29] and the generalized gradient approximation of Perdew, Burke, and Ernzerhof (PBE) [30]. For improved accuracy, particularly to improve the well-known band gap underestimate of LDA or PBE, the hybrid functional approach is used in the screened range-separated formulation by Heyd, Scuseria, and Ernzerhof (HSE) [31,32]. In all calculations, relaxed atomic configurations are determined with forces minimized typically to <20 meV/Å. Convergence with respect to the number of integration points in the Brillouin zone and the plane wave cutoff is checked. For localized charged defects, the Makov–Payne correction scheme [33] is applied to computed energies.

The analysis of point defect properties begins with the calculation of the defect formation energies, ΔE_f, which reveal the equilibrium concentrations of different defects as well as some of their electronic properties. The formation energy of a defect, D, in charge state, q, is given by

$$\Delta E_{f,D}(q) = E_D - E_{ideal} - \sum_i \Delta n_i \mu_i + q\mu_e, \quad (1)$$

where E_D is the total energy of the system containing the defect (with atomic relaxation included), E_{ideal} is the energy without the defect, Δn_i is the number of atoms of type i and chemical potential μ_i added to the system, and μ_e is the electron chemical potential (Fermi level) [34–39]. The μ_i terms also embed the chemical environment of the crystal. In Eq. (1), we neglect the contributions of vibrational entropy and pressure–volume terms to the energy, since these are small at ambient conditions. The equilibrium concentration of a given defect is $c_D(q) = c_0\, exp(-\Delta E_{f,D}(q)/k_BT)$, where c_0 is the site concentration (for the specific type of defect), k_B is Boltzmann's constant, and T is absolute temperature. By comparing the formation energies of different defects, we can determine which are most prevalent in the crystal. In addition, the last term in Eq. (1) indicates the linear dependence of ΔE_f on μ_e for charged defects, implying the possibility of regimes of μ_e within the material's band gap where a certain charge state of a defect is more favorable than another. These charge-state regimes and the values of μ_e where transitions between charge states occur reveal the donor, acceptor, or neutral nature of a defect and its associated shallow or deep electronic level (more detail is given below). Charge transitions near mid-gap represent strong carrier traps and degrade carrier lifetimes [40].

The effects of defects on carrier mobility can be predicted by computing the carrier scattering rate using perturbation theory [41–44]. We have shown that a good, rapidly computable relative measure of carrier scattering for defects with the same absolute charge state is given by [44]

$$M^2 = \left[\int |\nabla_{\mathbf{r}}(\Delta V)|\, d\mathbf{r}\right]^2, \quad (2)$$

where ΔV, the perturbation potential, is the difference of the self-consistent potential in the defect supercell compared to the perfect system. Larger values of M^2 are more detrimental to carrier mobility. This perturbative scheme also can be applied to study the scattering from phonons and alloy disorder [9,45,46].

Mass transport properties of the crystals are determined by computing the energy barrier for atoms (defects) to hop between lattice sites. The nudged elastic band method [47] allows this energy barrier to be estimated with DFT.

Further details of specific computations are given as needed in the discussions that follow. Additional details are also found in the cited references.

3. Point defects in Cd(Zn)Te

3.1. Native point defects in CdTe

We calculated the formation energies of native defects in CdTe—including vacancies, antisites, interstitials, and several complexes—using both LDA and an HSE-like hybrid functional (constructed using LDA instead of PBE) [6]. The calculated band gap of CdTe is 0.63 eV with LDA and 1.48 eV with the hybrid functional, compared to the experimental value of 1.5 eV. Finite-size errors were estimated by comparing calculations with different supercell sizes from 64 to 512 atoms, and convergence with respect to number of k-points and energy cutoff was carefully checked. For each defect, all possible sites and symmetries were compared to find the lowest energy configuration. In total, more than 20 defect configurations and more than 400 structures (including different supercell sizes and charge states) were calculated. Fig. 1 summarizes the formation energies of the most important defects in CdTe; Fig. 1(a) and (b) shows the LDA results, while Fig. 1(c) shows the hybrid functional results.

Since CdTe is a II–VI compound, defects tend to be either neutral or have ± 2 charge. For Cd-rich material, the dominant defects are the shallow double donor Cd interstitial Cd_i (T_d symmetry in a Cd neighborhood), the shallow double acceptor Cd vacancy V_{Cd} (T_d symmetry), and the deep double donor Te vacancy V_{Te} (T_d symmetry). For Te-rich material, which is more typical, the dominant defects are the V_{Cd}, the very deep double donor Te antisite Te_{Cd} (C_{3v} symmetry when neutral, T_d symmetry when $q=+2$), the Cd_i, and Te_i (split dumbbell on a Te site oriented along a ⟨110⟩ direction). The Te_{Cd} undergoes a Jahn–Teller [48,49] symmetry breaking and lifting of degeneracy when transitioning from the T_d ($q=+2$) to the C_{3v} ($q=0$) state; however, for practical purposes, Te_{Cd} exists in the neutral C_{3v} state, since the donor transition is extremely deep, close to the valence band maximum (VBM). The Te_i exists as a split interstitial; the tetrahedral interstitial configurations have formation energies more than 1.5 eV higher [see Fig. 1(b)]. Several split interstitials have similar formation energies within 0.5 eV, with a shallow potential energy landscape connecting them, but the lowest energy configuration is $(Te–Te)_{Te,\langle 110\rangle}$, whose structure is shown in Fig. 2 [6,8]. Previous theoretical calculations that only considered tetrahedral interstitials predicted the high formation energies of those configurations [50].

The crossing within the gap of the formation energies of V_{Cd}^{2-} and Cd_i^{2+}, which are the lowest formation energy charged native defects, has implications for self-compensation of the material and Fermi level pinning, since charge neutrality will force the Fermi level to remain near the crossing point [51]. From the position of the crossing point, we expect Cd-rich material to be highly resistive or slightly n-type, while Te-rich material would be moderately p-type. Highly resistive Te-rich material is often achieved by addition of Cl, In, or other dopants that complex with V_{Cd} to shift the point of Fermi level pinning toward mid-gap [52,53,13].

Our results show that isolated V_{Cd} is a shallow double acceptor. Some previous theoretical works [50,54–56] assign a second deep transition to V_{Cd} $(-/=)$ at about 0.2–0.4 eV above the VBM, which appears to originate from overcorrection of the spurious electrostatic interaction of the supercell approximation [6]. Analysis of the charge density associated with the vacancy in the −2 charge state in large supercells shows nearly complete delocalization,

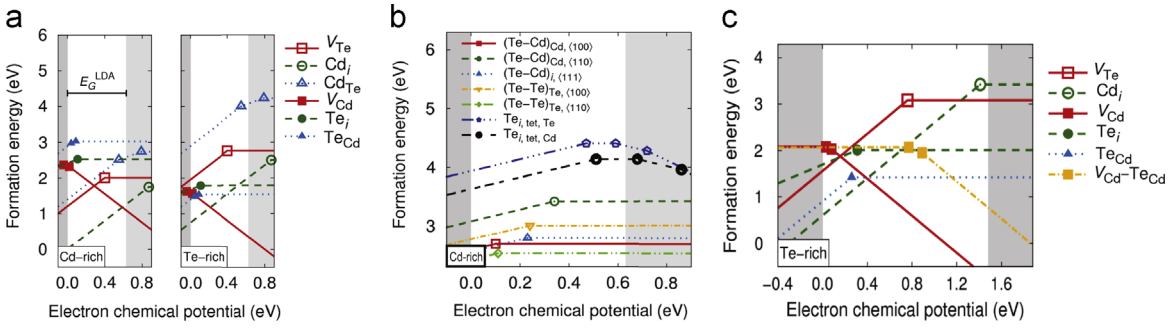

Fig. 1. (a) Formation energies for the most stable configuration of each native defect in CdTe, for both Cd-rich and Te-rich conditions, calculated using LDA. (b) LDA formation energies for the set of Te interstitial configurations, showing $(Te–Te)_{Te,\langle 110\rangle}$ as the most stable. (c) Formation energies calculated using a hybrid functional (LDA + 25% screened exact exchange) for the 5 most prevalent defects in CdTe and the V_{Cd}–Te_{Cd} complex, for Te-rich conditions.

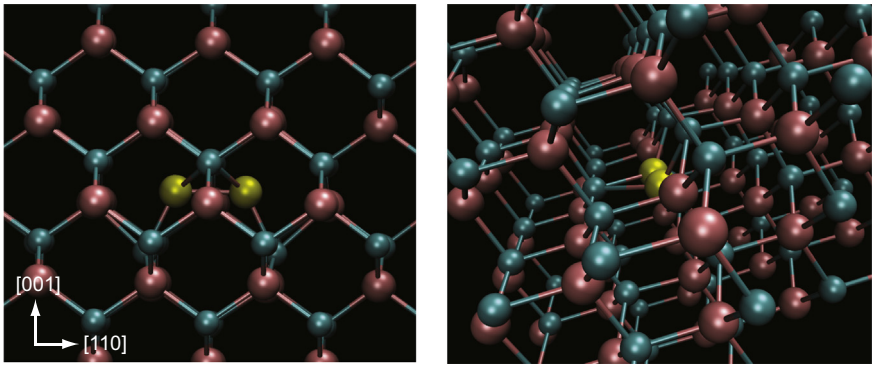

Fig. 2. Atomic structure of the $(Te–Te)_{Te,\langle 110\rangle}$ split interstitial in CdTe. Blue spheres = Cd, pink spheres = Te, yellow spheres = Te atoms comprising the interstitial. (From [8].) (For interpretation of the references to color in this figure caption, the reader is referred to the web version of this article.)

indicating a shallow defect. The experimental literature also shows a wide discrepancy of deep acceptor levels nominally assigned to V_{Cd}, including levels at approximately 0.2, 0.4, and 0.8 eV above the VBM [3,57–64,13,65]. One experiment reports a deep *donor* state for V_{Cd} at ~0.8 eV above the VBM [59]. The assignment to V_{Cd} often is made by comparing the presence or intensity of spectroscopic peaks between Cd-rich vs. Cd-poor material, and sometimes by comparing with the (previous) theoretical results. We interpret the experimental results as indicating the presence of V_{Cd}-*related* defects (defect complexes) that are not necessarily isolated vacancies. The most important native defect complex is the V_{Cd}–Te_{Cd}, which from Fig. 1(c) can be seen to be the only native deep acceptor we found. The level associated with this complex is predicted to occur at ~0.6 eV above the VBM with LDA and ~0.8 eV with the hybrid functional [6,7]. For Te-rich material, we determine by comparing the formation energies in Fig. 1(c) that a significant fraction, but not all, of the individual V_{Cd} and Te_{Cd} are expected to be complexed, with a concentration similar to that of Te_i.

The presence of the V_{Cd}–Te_{Cd} complex is predicted to be spectroscopically identifiable. We calculated the vibrational density of states for CdTe containing V_{Cd}, Te_{Cd}, and V_{Cd}–Te_{Cd} defects, using phonon calculations with the direct force approach and also verified with ab initio molecular dynamics simulations [7]. Fig. 3 shows the calculated spectra. The defect-related modes are both Raman and infrared active. In pure CdTe, distinct vibrational peaks for the different defects are present, however they may be difficult to resolve since they overlap the bulk CdTe vibrational spectrum. However, we find that hydrogen and/or deuterium doping makes the spectra quite distinct. The H/D impurities bind to Te atoms around the vacancy, producing high frequency vibrational modes with very different characteristics for isolated V_{Cd} compared to V_{Cd}–Te_{Cd}. Without the complex, the three vibrational modes

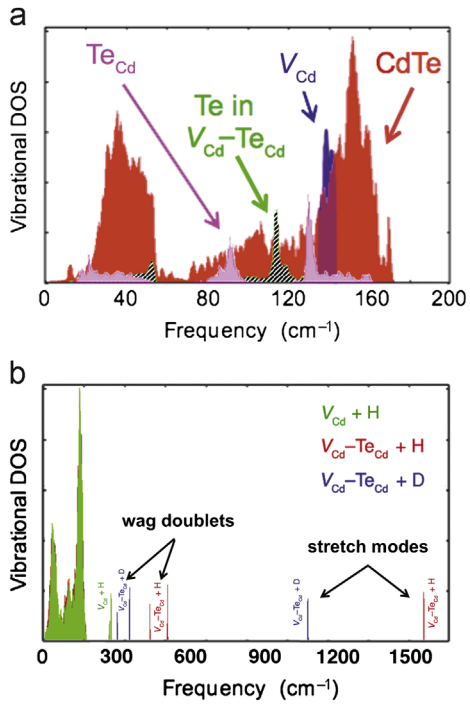

Fig. 3. (a) Vibrational density of states of CdTe, overlaid with the local mode spectra for V_{Cd}, Te_{Cd}, and V_{Cd}–Te_{Cd} defects, which are greatly exaggerated in amplitude for clarity. (b) Local mode spectra for V_{Cd} and V_{Cd}–Te_{Cd} decorated with H or D. Anharmonic effects related to the light mass of H have been neglected. (From [7].)

associated with H or D are nearly degenerate at ~300 cm^{-1} (green peaks). In the presence of the V_{Cd}-Te_{Cd} complex (red and blue peaks), the frequencies shift higher, with the two transverse wag modes splitting and the stretch mode appearing at a much higher frequency.

3.2. Zn alloy effects in CdZnTe

For room-temperature gamma detectors, Zn is usually added to CdTe to increase the band gap. At high temperatures, the alloy is fully miscible and melt growth results in a random alloy with Zn occupying a fraction of Cd sites. We studied the effect of Zn alloying on the defect properties using ensembles of randomly occupied supercells for compositions ranging from 5 to 13% Zn [9]. (Typical detector material contains ~10% Zn). Fig. 4(a) shows a typical result for the formation energies of native defects for the case of 8% Zn. We see that different defects vary in sensitivity to the Zn configuration for absolute formation energy and position of charge state transition levels. The two notable defects with significant dispersion due to alloy disorder are V_{Te} and Te_i. These are defects with very short-range structural and electronic order, which makes them sensitive to structural changes in their nearest-neighbors; the other defects average over configurations considerably farther from their center and see much less effect. The dispersion for these two defects is of little practical importance, since V_{Te} is rare and Te_i is neutral over all conditions relevant to radiation detectors. Furthermore, Fig. 4(b) shows that most defect formation energies are not sensitive to Zn composition either, except V_{Te} and Te_i. Therefore, CdTe is a good model for CZT, at least for moderate concentrations of Zn [9].

We further examined the carrier scattering properties of native defects as a function of Zn composition and alloy disorder, in addition to the thermodynamic properties and deep trap energies discussed above [9]. We found that point defect scattering was essentially identical to that in CdTe over the range of Zn compositions examined. However, alloy disorder contributes at least a factor of 2 more (up to an order of magnitude more) than point defect scattering in limiting carrier mobility for a reasonable concentration of defects. Alloy scattering shows a strong composition dependence, nearly doubling from 5 to 13% Zn. Nevertheless, thermal scattering was found to dominate both alloy and point defect scattering above ~150 K, so that at room temperature the carrier mobility is limited by phonons. Thus, impurity effects are relevant predominantly for limiting carrier lifetime in CZT rather than mobility.

3.3. Te clustering in Cd(Zn)Te

Cd(Zn)Te is grown slightly Te-rich to avoid phase separation during melt growth solidification due to retrograde solubility in the phase diagram near the melting point, which results in compositional inhomogeneity manifested as Te-rich regions or Te precipitates [13,66]. From the analysis in Section 3.1, we see that several native point defects present in the Te-rich material may contribute to formation of Te-rich regions in the crystal. The V_{Cd}^{2-} is by far the most prevalent defect at equilibrium, followed by Te_{Cd}^{0}. The $(Te–Te)_{Te,\langle 110\rangle}^{0}$ split interstitial (Te_i^0) also is present in appreciable concentration. The Cd_i^{2+} is present at similar concentrations as Te_i^0, but it is not important for clustering of Te. The V_{Te} is a very rare defect with a formation energy over 3 eV, so its effect is negligible. The relative rates of diffusion of these defects are estimated using the nudged elastic-band (NEB) method [47], which gives the saddle-point energy for migration of a defect to an adjacent lattice site. The diffusivity of the defect is proportional to $exp(-\Delta E_m/k_BT)$, where the migration energy barrier ΔE_m is the

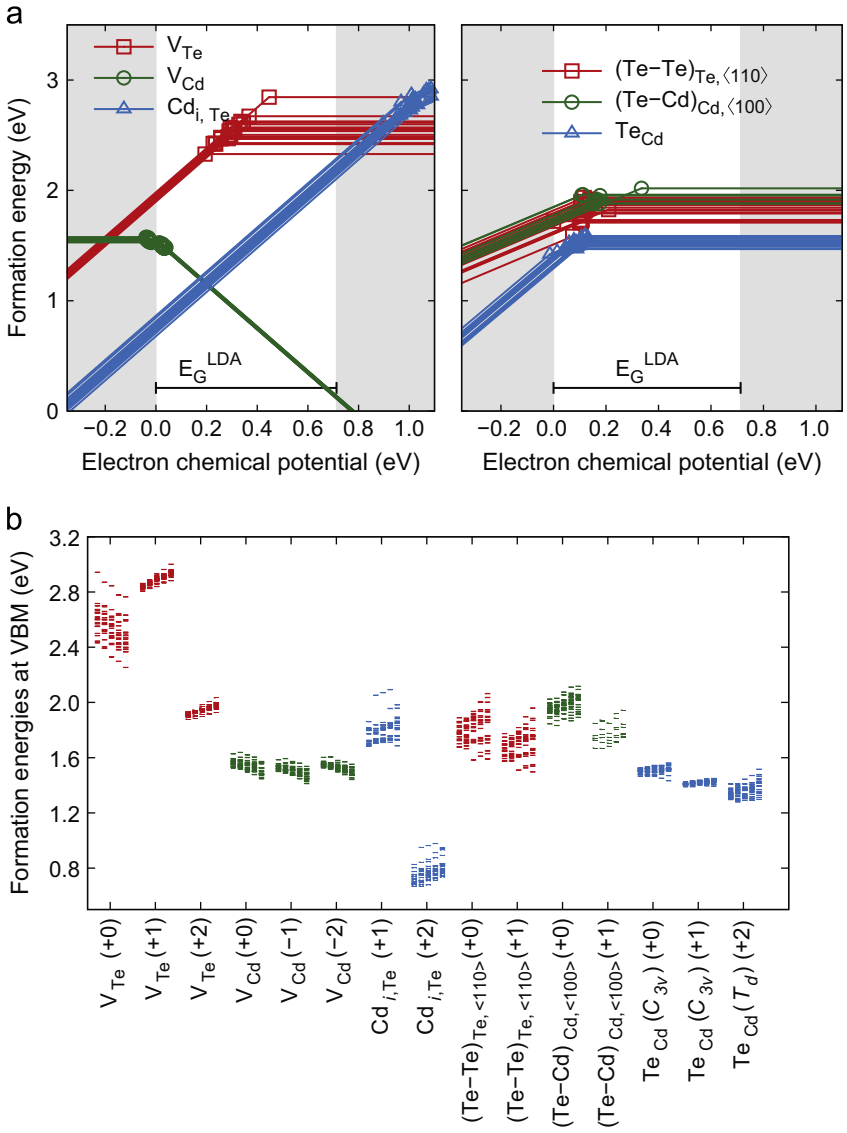

Fig. 4. (a) Variation of the LDA formation energies of major native defects with alloy configuration in $Cd_{0.12}Zn_{0.08}Te$. Each line corresponds to a different random Zn configuration. Compare to Fig. 1. (b) The formation energy at the VBM computed for 20 random Zn configurations at each of 5 concentrations from 5.5 to 13.0% Zn (left to right for each defect). (From [9].)

Table 1
Migration energy barriers for native defect diffusion in CdTe, calculated using LDA with 216-atom supercells and 6×6×6 *k*-points [8].

Process	Barrier (eV)
$(Te–Te)_{Te,\langle 110\rangle}$ migration along ⟨110⟩	0.16
$(Te–Te)_{Te,\langle 110\rangle}$ rotation 90°	0.26
$(Te–Te)_{Te,\langle 110\rangle}$ rotation 60°	0.47
V_{Cd}^{2-} migration	1.09
V_{Te}^{2+} migration	1.23
Te_{Cd}^{0} migration	1.68

difference between the energy of the saddle-point and the ground state. For each defect, the path of lowest ΔE_m is determined.

Table 1 shows the calculated migration energy barriers for diffusion of the relevant defects, as well as the barriers for rotation of the Te split interstitial between different ⟨110⟩ directions (e.g., [110] to [1$\bar{1}$0] is a 90° rotation, while [110] to [101] is 60°) [8]. The Te split interstitial is extremely mobile, with a very low barrier to shuffle along its direction of orientation and nearly as low a barrier to rotate to another ⟨110⟩ direction. The Te_{Cd} antisite has a high barrier and is essentially immobile except at the highest temperatures. V_{Cd} is in between. As a benchmark, at room temperature, barriers up to ~0.25 eV are highly mobile with RMS diffusion of 1 μm taking less than 1 s; at 1000 K, barriers up to 1.0 eV are mobile. At room temperature, a 0.5 eV barrier is moderately mobile, taking minutes to diffuse 1 μm, while > 1.0 eV is immobile, taking $> 10^{11}$ s; at 1000 K, a 1.6 eV barrier allows diffusion over 1 μm in minutes and 2.0 eV takes several hours.[1]

To study the clustering processes, we calculate the binding energy between defect pairs with [67]

$$\Delta E_{bind} = \Delta E_{f,complex} - \sum_i \Delta E_{f,i}, \tag{3}$$

where $\Delta E_{f,complex}$ is the formation energy of the complex (treated as a single entity in a supercell) and $\Delta E_{f,i}$ are the formation

[1] Attempt frequencies for the defect migration processes in CdTe are ~1 *THz* [8].

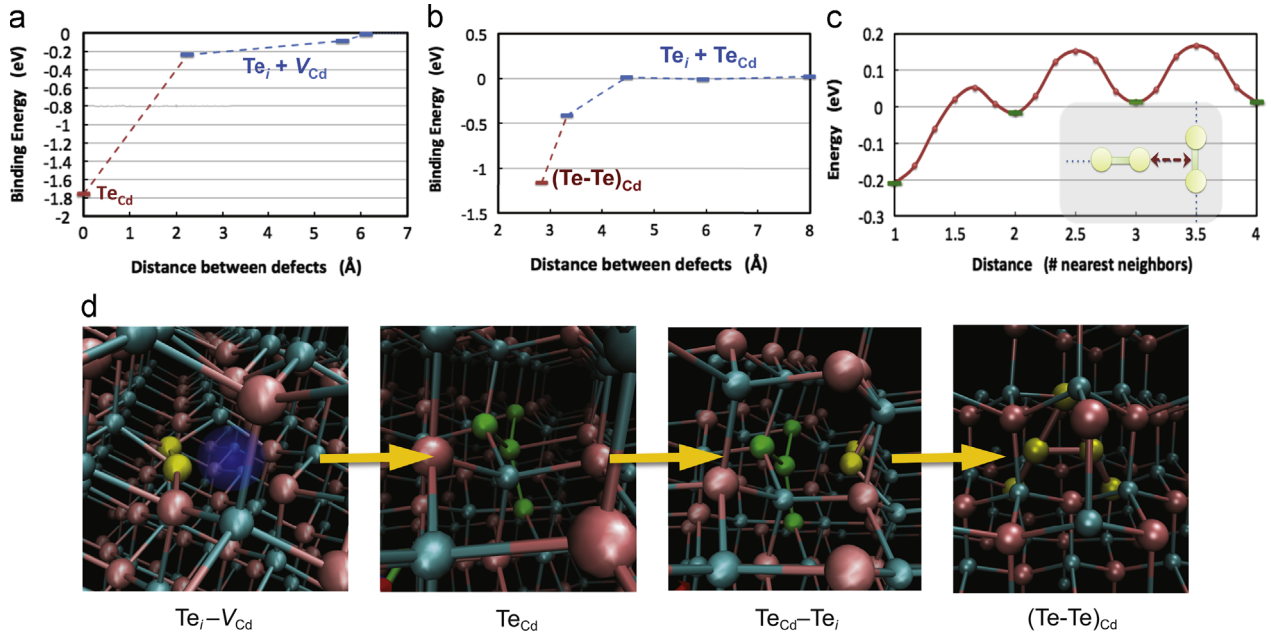

Fig. 5. (a) Binding energy for Te_i with V_{Cd} in CdTe shows conversion to Te_{Cd}. (b) Binding energy for Te_i with Te_{Cd} shows conversion to $(Te–Te)_{Cd}$. (c) Potential energy landscape for binding of perpendicularly oriented $(Te–Te)_{Te,\langle 110\rangle}$. (d) Schematic mechanism for Te clustering in CdTe via native point binding. (From [8].)

energies of the individual defects comprising the complex. Negative ΔE_{bind} denotes binding. Fig. 5(a)–(c) shows several calculated LDA binding energies as a function of separation between defects [8]. The V_{Cd}–Te_i complex binds by –0.25 eV, with a binding attraction from almost 6 Å away; once bound, however, the complex has a strong 1.6 eV driving force to combine and form a Te_{Cd} [Fig. 5(a)]. Similarly, Te_{Cd}–Te_i binds by –0.45 eV, with binding attraction from up to 4.5 Å away; as Te_i moves closer to Te_{Cd}, a barrierless transformation to $(Te–Te)_{Cd}$ occurs with 1.2 eV energy gain [Fig. 5(b)]. Pairs of Te_i are also bound, but the binding depends on the relative orientation between the split interstitials. When perpendicular, Te_i–Te_i bind by –0.2 eV in the first nearest neighbor (NN) position [Fig. 5(c)]. However, when brought together end-on, the first NN position is repulsive by 0.3 eV, with weak –0.05 eV binding in the second NN position; similarly, the parallel configuration is repulsive by 0.04 eV in the first NN position and weakly attractive (–0.03 eV) in the second NN position (not shown).

Therefore, a mechanistic pathway emerges, as schematized in Fig. 5(d): (i) the highly mobile Te_i diffuse through the crystal to the highly prevalent V_{Cd} and generate immobile Te_{Cd} (–1.6 eV); (ii) then Te_{Cd} attract additional Te_i, forming $(Te–Te)_{Cd}$ (–1.2 eV). The latter defect is a highly Te-rich cluster of 5 Te atoms in a triangular arrangement as shown in Fig. 5(d). In addition, weak binding (~0.2 eV) occurs between perpendicularly oriented Te_i; however these bound complexes may be short lived at elevated temperatures due to the small binding energy. Further details are in [8].

4. Defects and doping in TlBr

In TlBr, vacancies are the dominant native defect and are indeed a dominant factor for many of its electronic properties [10,11,68]. Fig. 6 shows the calculated formation energies of the native vacancies and antisites in TlBr as a function of Fermi level [10,11]. The calculations were performed using 128- and 250-atom supercells with the PBE functional and 54-atom supercells with HSE06 for comparison. Several features are clear: (i) vacancies are always the dominant native defect, (ii) the

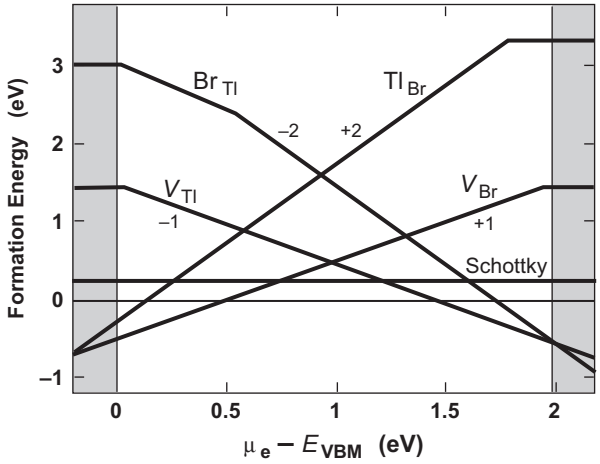

Fig. 6. Formation energies of native point defects in TlBr as a function of electron chemical potential (Fermi level) throughout the band gap (the PBE calculated band gap is denoted between the shaded regions). The slope of the lines denotes the charge state q, as per Eq. (1).

formation energies of vacancies are very low, (iii) the vacancies are always singly charged species (like the host atoms), (iv) the formation energies of the two oppositely charged vacancies cross near mid-gap, and (v) the formation energies of the vacancies become negative for values of the Fermi level within the band gap and not far from mid-gap. The implications are that the vacancies provide charge compensation in the material and pin the Fermi level near mid-gap (at the crossing point), maintaining high resistivity by denying electronic doping. Charge neutrality in the pure crystal is maintained by an equal concentration of V^+_{Br} and V^-_{Tl}. In fact, the stable configuration is bound Schottky pairs of V^-_{Tl} and V^+_{Br}. Attempts to shift the Fermi level toward, e.g., the valence band by doping with holes (with an extrinsic acceptor) leads to an exponential increase of the compensating V^+_{Br} concentration and thus resistance to Fermi level shift; similarly for doping with electrons, with V^-_{Tl} compensating. Thus, the Fermi level remains pinned very close to the mid-gap position where the vacancy formation energies cross. Theoretically, the maximum range of the

Fermi level is bounded by the points where the vacancy formation energies become negative, since at those points the concentration of vacancies would equal the number of lattice sites (within the dilute approximation used here); however, the auto-compensation keeps the Fermi level in a much narrower range in practice. Furthermore, since the formation energy of the vacancies is much lower than the electronic excitation energy ($\approx E_{gap}/2$), extrinsic dopants lead to the generation of charge-compensating vacancies rather than free carriers. Thus, TlBr cannot have a significant free carrier concentration and resists carrier doping, maintaining high resistivity. Similarly, near-stoichiometry is always maintained, except with extreme levels of an extrinsic dopant.

Since no native defects have charge transition levels within the band gap, the pure material exhibits very long carrier lifetimes due to the lack of carrier trapping centers. This property is maintained as long as impurities that introduce mid-gap states are avoided. The measured large $\mu\tau$ in high-quality TlBr is a result of the long carrier lifetime. In fact, the material suffers from low carrier mobilities, even when ultrapurified [69–71,19]. Theoretically, we can expect the mobility at room temperature to be limited by scattering from phonons since the Debye temperature is only ~160 K. We estimated the phonon-limited electron and hole mobilities as a function of temperature using a scattering model and deformation potentials calculated with DFT [10]. For temperatures above ~200 K we get good agreement with measured mobilities from highly purified material [72], confirming that the low mobilities at room temperature (about 40 and 10 $cm^2/V\,s$ for electrons and holes, respectively [70,72]) are phonon limited and will not be increased with further purification. Consequently, for detector material development, careful attention must be paid to avoid the introduction of any trapping centers that will reduce lifetimes, although scattering centers are not a concern for degrading mobilities.

Another important implication of the high concentration of vacancies in TlBr is the mediation of ionic transport. Diffusion of Tl^+ and Br^- ions occurs via a vacancy hop mechanism, expressed via

$$D = fs^2\nu p_i p_f = fa_0^2\left[\nu_0\, exp\left(\frac{-\Delta E_m}{k_B T}\right)\right]\left[exp\left(\frac{-\Delta E_f^{vac}}{k_B T}\right) + \tilde{n}_{vac}^{excess}\right], \qquad (4)$$

where D is the diffusivity, f is a geometrical correlation coefficient, s is the hop distance, ν is the vacancy exchange rate, p_i is the probability of occupying an initial site, and p_f is the probability of finding a neighboring vacancy into which to hop [73]. For TlBr, which has a CsCl structure, diffusion occurs along ⟨100⟩ directions with simple cubic hopping, thus $f=0.655$ and $s = a_0 = 4.056$ Å. The vacancy exchange rate is thermally activated and expressed as $\nu = \nu_0\, exp(-\Delta E_m/k_B T)$, where ΔE_m is a migration energy barrier and ν_0 is an attempt frequency, or the frequency of vibration in the direction of the vacancy. Since the concentration of vacancies is much less than 1, $p_i \approx 1$ and p_f is given by the normalized vacancy concentration, which is expressed as a sum of the normalized equilibrium concentration given by the formation energy and a normalized excess concentration of vacancies, $\tilde{n}_{vac}^{excess}$. This last term accounts for the possibility of a non-equilibrium concentration of vacancies. Both Tl^+ and Br^- diffuse via their respective vacancies as described by Eq. (4). The drift mobility of each ion is given by $\mu_j = qD_j/k_B T$, from which an ionic current as the sum of the contributions of both ions is developed when an electric field is applied across the crystal.

The parameters in Eq. (4) can be calculated with DFT, providing a first-principles prediction of ionic current in the material as a function of temperature and excess vacancy concentration. As described above, charged impurities are compensated by production of oppositely charged vacancies in TlBr, so a non-equilibrium concentration of vacancies can be associated with either freeze-in from cooling during melt growth or the presence of charged impurities. The vacancy formation energy is calculated via Eq. (1). To calculate ΔE_m and ν_0, we use the nudged elastic band (NEB) method [47] with DFT. NEB samples the minimum energy pathway (MEP) on the potential energy surface for migration of an ion (exchange with a neighboring vacancy of the same type). The saddle point connecting the starting and ending configurations is the transition state of the MEP and provides the migration energy barrier. Fig. 7 shows the MEPs for migration of V_{Tl}^- and V_{Br}^+ calculated using 128-atom supercells and PBE, from which $\Delta E_{m,V_{Tl}^-} = 0.31$ eV and $\Delta E_{m,V_{Br}^+} = 0.10$ eV are extracted. The ν_0 term is formally obtained from transition state theory via the Vineyard equation [74], which equates ν_0 to the ratio of the products of stable vibrational modes in the ground state and transition state. In the case of TlBr vacancy migration, where only the single vibrational degree of freedom in the direction of motion dominates, ν_0 can be extracted from a harmonic approximation of the bottom of the MEP. This procedure yields $\nu_{0,V_{Tl}} = 0.43$ THz and $\nu_{0,V_{Br}} = 0.38$ THz [11], close to the short-wavelength frequency of the transverse acoustic phonon in the X direction. The excess vacancy concentration $\tilde{n}_{vac}^{excess}$ in Eq. (4) is treated as a free parameter.

We see that V_{Br}^+ are much more mobile than V_{Tl}^-. Using the calculated parameters, the intrinsic mobilities of Br^- and Tl^+ at room temperature are, respectively, in the order of 10^{-12} and $10^{-15}\,cm^2/V\,s$. These values correspond to a room-temperature ionic conductivity of $3\times10^{-9}\,\Omega^{-1}\,cm^{-1}$ or a current density of $3\,\mu A/cm^2$ with 1000 V/cm applied electric field. For illustration, we compute the time for Br^- to drift 1 mm in an electric field of 1000 V/cm (typical for detectors) at room temperature with different V_{Br} concentrations: for the equilibrium concentration, it would take 270 years; for $10^{17}\,cm^{-3}$ excess V_{Br}, ~1 year; for $>10^{18}\,cm^{-3}$ excess, days. These estimates are lower bounds, since the calculated ΔE_m are slightly underestimated. At room temperature, at least 10^{15}–$10^{17}\,cm^{-3}$ excess vacancies are required to affect the ionic mobility [11]. In real crystals, additional sources and sinks for vacancies, such as dislocations, may need to be considered; high quality crystals usually have a low dislocation density, but mechanical deformation of this soft material can generate dislocations.

With high concentrations of highly mobile vacancies being associated with background ionic current and possibly the polarization phenomenon in TlBr, we want to assess whether doping could be used to trap vacancies and reduce their mobility. This would also reduce the required purity of the material, since the

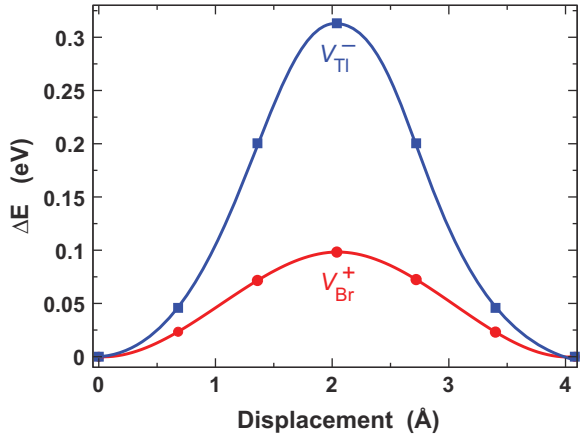

Fig. 7. Minimum energy pathways for vacancy migration in TlBr calculated using the climbing image nudged elastic-band method with DFT–PBE.

presence of charged impurities is associated with excess vacancies. The concept of doping to trap mobile vacancies relies on the ability to form stable neutral complexes, since $q=0$ defects have no mobility and do not contribute to drift current. A neutral dopant–vacancy complex would need to be bound sufficiently strongly to resist separation into two charged defects under the action of an electric field. Furthermore, the trapping must be accomplished without impacting the favorable electronic properties of TlBr that make it a good room-temperature detector, namely the very long carrier lifetime; therefore, deep levels must not be introduced by the doping.

We screened several possible dopants, including Sn, Pb, S, Se, and Te [10]. The binding energies of dopant–vacancy complexes are calculated from Eq. (3). We find that Pb, which substitutes Tl as Pb_{Tl}^{+}, binds strongly to V_{Tl}^{-}; S, Se, and Te, which substitute Br as X_{Br}^{-}, each bind to V_{Br}^{+}. All of these complexes have binding energies of −0.4 to −0.5 eV, which are compared to −0.36 eV for the Schottky pair. In addition, all four of these complexes are neutral and none, except for Te, introduce any detrimental deep levels. However, doping the system with any one of these will not reduce the ionic conductivity because the unbalanced neutralization of one vacancy over the other will drive the generation of additional vacancies to maintain charge neutrality, which actually enhances the conductivity. This problem can be solved by co-doping with equal concentrations of acceptor and donor dopants, such as Pb + S or Pb + Se. Our calculations show that the stable configuration of these two co-doped systems is a compact four-center complex consisting of the donor (Pb), acceptor (S or Se), and both vacancies (V_{Tl} and V_{Br}) arranged in a square-like configuration (see Fig. 8), with binding energies of −1.43 and −1.29 eV for the S and Se complexes, respectively [10]. A concentration of dopants comparable to the vacancy concentration is required to appreciably reduce the ionic conductivity, which implies a reasonable doping range of $\sim 10^{14}$–10^{18} cm^{-3}, depending on how close the material is to intrinsic. Since these complexes are relatively large objects, we calculate their carrier scattering strengths to ensure that carrier mobility is not affected. We find that the M^2 from Eq. (2) is less than 3× that of the native Schottky pair, which is not large enough to affect carrier mobility, since it is dominated by phonon scattering that is more than an order of magnitude higher.

5. Summary

We have presented several examples of the application of first-principles theoretical methods to understand fundamental defect properties relevant to the fabrication of high-performance room-temperature radiation detectors. The examples focused on two leading materials for this application, namely Cd(Zn)Te and TlBr.

Analysis of the native defects in Cd(Zn)Te revealed a dominant role of V_{Cd}, as well as the importance of the V_{Cd}–Te_{Cd} native deep acceptor complex. Isolated V_{Cd} was shown to be only a shallow acceptor. The thermodynamically favorable structure of the Te interstitial was shown to be the $(Te–Te)_{Te,\langle 110\rangle}$ split interstitial, which is extremely mobile throughout the crystal. The split interstitial can easily shuffle along its oriented ⟨110⟩ direction as well as rotate to other orientations. Diffusion of the Te_i was shown to lead to Te clustering through a multi-step mechanism involving binding to V_{Cd}, formation of Te_{Cd}, binding to Te_{Cd}, and formation of $(Te–Te)_{Cd}$. V_{Cd} is much less mobile than Te_i, and Te_{Cd} is immobile. Furthermore, the effects of Zn alloying in CdZnTe were shown to be weak for modifying the thermodynamic and electronic properties of point defects, confirming that CdTe is a good computational model for CZT. The main effects of Zn alloying are to increase the band gap and reduce the low-temperature carrier mobility, but above ~150 K, the carrier mobility in CZT is dominated by phonon scattering.

Analysis of the native defects in TlBr revealed a special role of charged vacancies, which serve to self-compensate the material and maintain high resistivity and near-stoichiometry. The lack of native deep traps gives TlBr extremely long carrier lifetimes, enabling the material to be used for high energy-resolution detectors even with low intrinsic carrier mobilities. However, the large concentration of charged vacancies, which mediate ionic transport in the crystal, lead to background ionic noise currents in detectors. These background ionic currents may be time dependent and contribute to detector degradation over time. A co-doping scheme was presented to trap vacancies and reduce the ionic conductivity in TlBr, reducing the sensitivity of the electronic properties to impurities. The co-doping, which relies on strong binding between the dopants and both vacancies, allows independent control over the electronic and ionic conductivities in the material.

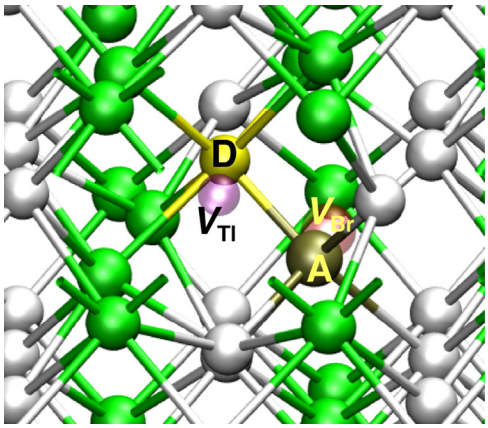

Fig. 8. Atomic structure of co-dopants–vacancies complex in TlBr. White spheres are Tl, green spheres are Br, and the defect sites are labeled (D=donor, A=acceptor). (From [10].) (For interpretation of the references to color in this figure caption, the reader is referred to the web version of this article.)

Acknowledgments

The author gratefully acknowledges contributions from Cedric Rocha Leão, Daniel Åberg, and Paul Erhart. This work was performed under the auspices of the U.S. Department of Energy by Lawrence Livermore National Laboratory under Contract DE-AC52-07NA27344, with support from the National Nuclear Security Administration Office of Nonproliferation and Verification Research and Development NA-22.

References

[1] G.F. Knoll, Radiation Detection and Measurement, 4th ed., Wiley, 2010.
[2] S. Del Sordo, L. Abbene, E. Caroli, A.M. Mancini, A. Zappettini, P. Ubertini, Sensors 9 (2009) 3491–3526.
[3] M. Hage-Ali, P. Siffert, in: T. Schlesinger, R. James (Eds.), Semiconductors and Semimetals, vol. 43, Academic Press, New York, 1995, p. 219.
[4] A. Owens, Journal of Synchrotron Radiation 13 (2006) 143–150.
[5] G.A. Armantrout, S.P. Swierkowski, J.W. Sherohman, J.H. Lee, IEEE Transactions on Nuclear Science NS-24 (1977) 121–125.
[6] P. Erhart, D. Åberg, V. Lordi, Intrinsic point defects in cadmium telluride studied using hybrid density-functional theory calculations, in preparation.
[7] V. Lordi, Native deep acceptor complexes in CdTe, in preparation.
[8] V. Lordi, Mechanism of Te clustering in CdTe, in preparation.
[9] D. Åberg, P. Erhart, V. Lordi, Contributions of point defects, chemical disorder, and thermal vibrations to electronic properties of $Cd_{1-x}Zn_xTe$ alloys, in preparation.
[10] C.R. Leão, V. Lordi, Physical Review Letters 108 (2012) 246604.
[11] C.R. Leão, V. Lordi, Physical Review B 87 (2013) 081202(R).
[12] R. Redus, J. Pantazis, T. Pantazis, A. Huber, B. Cross, IEEE Transactions on Nuclear Science 56 (2009) 2524–2532.

[13] T. Schlesinger, J. Toney, H. Yoon, E. Lee, B. Brunett, L. Franks, R. James, Material Science and Engineering: R: Reports 32 (2001) 103–189.
[14] A. Melnikov, A. Sigov, K. Vorotilov, A. Davydov, L. Topalova, Journal of Crystal Growth 197 (1999) 666.
[15] F. Zhang, Z. He, D. Xu, G. Knoll, D. Wehe, J. Berry, IEEE Transactions on Nuclear Science 51 (2004) 2427–2431.
[16] S.A. Awadalla, H. Chen, J. Mackenzie, P. Lu, K. Iniewski, P. Marthandam, R. Redden, G. Bindley, Z. He, F. Zhang, M. Groza, A. Burger, D.R. Mayo, C.L. Sullivan, in: Nuclear Science Symposium Conference Record, 2008. NSS '08. IEEE, pp. 58–62.
[17] M. Shorohov, M. Kouznetsov, I. Lisitskiy, V. Ivanov, V. Gostilo, A. Owens, IEEE Transactions on Nuclear Science 56 (2009) 1855.
[18] K. Hitomi, M. Matsumoto, O. Muroi, T. Shoji, Y. Hiratate, IEEE Transactions on Nuclear Science 49 (2002) 2526.
[19] A. Churilov, G. Ciampi, H. Kim, L. Cirignano, W. Higgins, F. Olschner, K. Shah, IEEE Transactions on Nuclear Science 56 (2009) 1875–1881.
[20] K. Hitomi, Y. Kikuchi, T. Shoji, K. Ishii, IEEE Transactions on Nuclear Science 56 (2009) 1859.
[21] K. Hitomi, T. Shoji, Y. Nlizeki, Nuclear Instruments and Methods in Physics Research Section A 585 (2008) 102–104.
[22] P.E. Blöchl, Physical Review B 50 (1994) 17953–17979.
[23] G. Kresse, D. Joubert, Physical Review B 59 (1999) 1758–1775.
[24] G. Kresse, J. Hafner, Physical Review B 47 (1993) 558–561.
[25] G. Kresse, J. Hafner, Physical Review B 49 (1994) 14251.
[26] G. Kresse, J. Furthmüller, Physical Review B 54 (1996) 11169.
[27] G. Kresse, J. Furthmüller, Computational Material Science 6 (1996) 15–50.
[28] U. von Barth, L. Hedin, Journal of Physics C: Solid State Physics 5 (1972) 1629–1642.
[29] D.M. Ceperley, B.J. Alder, Physical Review Letters 45 (1980) 566–569.
[30] J.P. Perdew, K. Burke, M. Ernzerhof, Physical Review Letters 77 (1996) 3865–3868.
[31] J. Heyd, G. Scuseria, M. Ernzerhof, Journal of Chemical Physics 118 (2003) 8207–8215.
[32] J. Heyd, G. Scuseria, M. Ernzerhof, Journal of Chemical Physics 124 (2006) 219906.
[33] G. Makov, M.C. Payne, Physical Review B 51 (1995) 4014–4022.
[34] G.-X. Qian, R.M. Martin, D.J. Chadi, Physical Review B 38 (1988) 7649.
[35] S.B. Zhang, J.E. Northrup, Physical Review Letters 67 (1991) 2339–2342.
[36] C. Persson, Y.-J. Zhao, S. Lany, A. Zunger, Physical Review B 72 (2005) 035211.
[37] D. Åberg, P. Erhart, A.J. Williamson, V. Lordi, Physical Review B 77 (2008) 165206.
[38] P. Erhart, D. Åberg, V. Lordi, Physical Review B 81 (2010) 195216.
[39] S. Lany, A. Zunger, Physical Review B 78 (2008) 235104.
[40] W. Shockley, W. Read Jr., Physical Review 87 (1952) 835–842.
[41] D. Chattopadhyay, H. Queisser, Reviews of Modern Physics 53 (1981) 745.
[42] M. Fischetti, S. Laux, Journal of Applied Physics 80 (1996) 2234.
[43] M.H. Evans, X.-G. Zhang, J. Joannopoulos, S. Pantelides, Physical Review Letters 95 (2005) 106802.
[44] V. Lordi, P. Erhart, D. Åberg, Physical Review B 81 (2010) 235204.
[45] O.D. Restrepo, K. Varga, S. Pantelides, Applied Physical Letters 94 (2009) 212103.
[46] F. Murphy-Armando, S. Fahy, Physical Review Letters 97 (2006) 096606.
[47] G. Henkelman, B.P. Uberuaga, H. Jónsson, Journal of Chemical Physics 113 (2000) 9901–9904.
[48] H.A. Jahn, E. Teller, Proceedings of the Royal Society of London A 161 (1937) 220–235.
[49] I. Bersuker, The Jahn–Teller Effect, Cambridge University Press, 2010.
[50] S.-H. Wei, S.B. Zhang, Physical Review B 66 (2002) 155211.
[51] S.B. Zhang, S.-H. Wei, A. Zunger, Physical Review B 63 (2001) 075205.
[52] D.M. Hofmann, P. Omling, H.G. Grimmeiss, B.K. Meyer, K.W. Benz, D. Sinerius, Physical Review B 45 (1992) 6247–6250.
[53] M. Fiederle, V. Babentsov, J. Franc, A. Fauler, J.-P. Konrath, Crystal Research and Technology 38 (2003) 588–597.
[54] S. Wei, S.B. Zhang, A. Zunger, Journal of Applied Physics 87 (2000) 1304.
[55] Y.-C. Chang, R.B. James, J.-W. Davenport, Physical Review B 73 (2006) 035211.
[56] P. Jakubas, P. Boguslawski, Physical Review B 77 (2008) 214104.
[57] A. Castaldini, A. Cavallini, B. Fraboni, P. Fernandez, J. Piqueras, Journal of Applied Physics 83 (1998) 2121.
[58] C. Szeles, Y. Shan, K. Lynn, A. Moodenbaugh, E. Eissler, Physical Review B 55 (1997) 6945.
[59] Z. Huang, E. Eissler, C. Wie, Nuclear Instruments and Methods in Physics Research Section B 100 (1995) 507.
[60] B.K. Meyer, D.M. Hofmann, Applied Physics A: Materials Science and Processing 61 (1995) 213.
[61] P. Emanuelsson, P. Omling, B.K. Meyer, M. Wienecke, M. Schenk, Physical Review B 47 (1993) 15578.
[62] U. Reislöhner, J. Grillenberger, W. Witthuhn, Journal of Crystal Growth 184–185 (1998) 1160.
[63] N. Krsmanovic, K.G. Lynn, M.H. Weber, R. Tjossem, T. Gessmann, C. Szeles, E. E. Eissler, J.P. Flint, H.L. Glass, Physical Review B 62 (2000) R16279.
[64] R. Soundararajan, K.G. Lynn, S. Awadallah, C. Szeles, S.-H. Wei, Journal of Electronic Materials 35 (2006) 1333.
[65] A. Carvalho, A.K. Tagantsev, S. Öberg, P.R. Briddon, N. Setter, Physical Review B 81 (2010) 075215.
[66] R. James, B. Brunett, J. Heffelfinger, J. Van Scyoc, J. Lund, F. Doty, C. Lingren, R. Olsen, E. Cross, H. Hermon, H. Yoon, N. Hlton, M. Schieber, E. Lee, J. Toney, T. Schlesinger, M. Goorsky, W. Yao, H. Chen, A. Burger, Journal of Electronic Materials 27 (1998) 788.
[67] C.G. Van de Walle, J. Neugebauer, Journal of Applied Physics 95 (2004) 3851–3879.
[68] M.-H. Du, Journal of Applied Physics 108 (2010) 053506.
[69] K. Hitomi, T. Onodera, T. Shoji, Nuclear Instruments and Methods in Physics Research Section A: Accelerators, Spectrometers, Detectors and Associated Equipment 579 (2007) 153–156.
[70] K. Hitomi, M. Matsumoto, O. Muroi, T. Shoji, Y. Hiratate, Journal of Crystal Growth 225 (2001) 129–133.
[71] F. Olschner, K. Shah, J. Lund, J. Zhang, K. Daley, S. Medrick, M. Squillante, Nuclear Instruments and Methods in Physics Research Section A: Accelerators, Spectrometers, Detectors and Associated Equipment 322 (1992) 504–508.
[72] T. Kawai, K. Kobayashi, M. Kurita, Y. Makita, Journal of the Physical Society of Japan 30 (1971) 1101.
[73] P. Knauth, H. Tuller, Journal of the American Ceramic Society 85 (2002) 1654–1680.
[74] G. Vineyard, Journal of Physics and Chemistry of Solids 3 (1957) 121.